Original Article

Qualitative and quantitative imaging features of pulmonary subsolid nodules: differentiating invasive adenocarcinoma from minimally invasive adenocarcinoma and preinvasive lesions

Linlin Qi[1], Wenwen Lu[2], Lin Yang[3], Wei Tang[1], Shijun Zhao[1], Yao Huang[1], Ning Wu[1,4], Jianwei Wang[1]

[1]Department of Diagnostic Radiology, National Cancer Center/National Clinical Research Center for Cancer/Cancer Hospital, Chinese Academy of Medical Sciences and Peking Union Medical College, Beijing 100021, China; [2]Department of Ophthalmology, Beijing Key Laboratory of Restoration of Damaged Ocular Nerve, Peking University Third Hospital, Beijing 100191, China; [3]Department of Diagnostic Pathology, [4]PET-CT Center, National Cancer Center/National Clinical Research Center for Cancer/Cancer Hospital, Chinese Academy of Medical Sciences and Peking Union Medical College, Beijing 100021, China

Contributions: (I) Conception and design: J Wang; (II) Administrative support: N Wu; (III) Provision of study materials or patients: J Wang, N Wu; (IV) Collection and assembly of data: L Qi, W Lu; (V) Data analysis and interpretation: L Qi, W Lu, L Yang, W Tang; (VI) Manuscript writing: All authors; (VII) Final approval of manuscript: All authors.

Correspondence to: Jianwei Wang. Department of Diagnostic Radiology, National Cancer Center/National Clinical Research Center for Cancer/Cancer Hospital, Chinese Academy of Medical Sciences and Peking Union Medical College, No. 17 Panjiayuan Nanli, Chaoyang District, Beijing 100021, China. Email: dr_jianweiwang@sina.com; Ning Wu. Department of Diagnostic Radiology & PET-CT Center, National Cancer Center/National Clinical Research Center for Cancer/Cancer Hospital, Chinese Academy of Medical Sciences and Peking Union Medical College, No. 17 Panjiayuan Nanli, Chaoyang District, Beijing 100021, China. Email: cjr.wuning@vip.163.com.

Background: To explore the role of qualitative and quantitative imaging features of pulmonary subsolid nodules (SSNs) in differentiating invasive adenocarcinoma (IAC) from minimally invasive adenocarcinoma (MIA) and preinvasive lesions.

Methods: We reviewed the clinical records of our institute from October 2010 to December 2015 and included 316 resected SSNs from 287 patients: 260 pure ground-glass nodules, 47 part-solid nodules with solid components ≤5 mm, and 9 ground-glass nodules (GGNs) with cystic airspaces. According to the pathologic review results, 307 SSNs in addition to nine GGNs with cystic airspaces were divided into two groups: A, including atypical adenomatous hyperplasia (AAH) (n=15), adenocarcinoma in situ (AIS) (n=56), and MIA (n=41); B, including 195 IACs. Univariate and binary logistic regression analyses were conducted to identify independent risk factors for IAC.

Results: Univariate analysis showed significant differences between groups regarding patient age, mean diameter, mean and relative computed tomography (CT) values, volume, mass (all P<0.001), and morphological features including lobulated sign (P<0.001), spiculated sign (P=0.028), vacuole sign/air bronchogram (P<0.001), and pleural retraction (P=0.017). Binary logistic regression and receiver operating characteristic analysis indicated the SSN mass as the only independent risk factor of IAC (odds ratio, 1.007; P<0.001), with an optimal cutoff value of 283.2 mg [area under curve (AUC): 0.859; sensitivity: 68.7%; specificity: 92.9%]. Among lepidic, acinar, and papillary adenocarcinomas, we found significant differences for the vacuole sign/air bronchogram (P=0.032) and mean and relative CT values (P<0.001). All nine GGNs with cystic airspaces were IACs.

Conclusions: The SSN mass with an optimal cutoff value of 283.2 mg may be reliable for differentiating IAC from MIA and preinvasive lesions.

Keywords: Solitary pulmonary nodule; lung neoplasms; adenocarcinoma in situ (AIS); tomography, X-ray computed; logistic regression

Submitted Sep 10, 2019. Accepted for publication Nov 12, 2019.
doi: 10.21037/jtd.2019.11.35
View this article at: http://dx.doi.org/10.21037/jtd.2019.11.35

Introduction

Lung cancer is the leading cause of cancer-related mortality (1). With the application of multi-detector computed tomography (CT) and development of low-dose CT for lung cancer screening, subsolid nodules (SSNs) have been increasingly detected, especially among Asian women and non-smokers (2,3). SSNs are divided into two subtypes: part-solid nodules (PSNs) and pure ground-glass nodules (pGGNs) (4). Ground-glass opacity (GGO) is defined as a hazy increased opacity of the lung, with preservation of the bronchial and vascular margins on high-resolution CT (HRCT) (5). GGOs can be a manifestation of inflammation, infection, or fibrosis, but several studies have shown that persistent SSNs, barring a few exceptions, pathologically represent invasive pulmonary adenocarcinoma or its pre-invasive lesions (6-8).

Patients with adenocarcinoma *in situ* (AIS) or minimally invasive adenocarcinoma (MIA) who undergo complete resection should have 100% or near 100% 5-year disease-free survival, respectively (4,9). Boland *et al.* (9) reported that the 10-year disease-specific survival (DSS) for AIS determined by two observers was 100%, while the 10-year DSS for MIA was 97.3% for observer 1 and 97.6% for observer 2. Patients with AIS and MIA experience excellent DSS. Furthermore, studies have shown that pGGNs suspected pathologically to be AIS or MIA can be considered for close follow-up or limited resection (segmental or wedge resection), while lobectomy is still considered as the standard surgical treatment for invasive adenocarcinoma (IAC) (10,11). Therefore, prediction of IAC likelihood among patients with SSNs would be very helpful in deciding the optimal management and evaluating prognosis.

Many previous studies have been conducted to reveal the correlation between histological types or invasiveness and CT findings in SSNs through qualitative, semi-quantitative or quantitative measurements (12-28). However, to our knowledge, only few studies have explored the correlation between histological types and SSN volume or mass (22). Three-dimensional volumetric and mass analyses have been reported to reflect the true growth of SSNs with acceptable reproducibility (29,30). Indeed, mass measurements may simultaneously reflect SSN volume and density, potentially having superior reproducibility to three-dimensional volumetry (31).

In this study, we used a computer-aided volumetry software (Lung VCAR AW 4.6; GE HealthCare, Milwaukee, WI) to measure volumes of SSNs automatically and accurately. Further, the qualitative and quantitative imaging features of pulmonary SSNs were all taken into consideration. Our purpose was to explore the efficiency of such features in differentiating IAC from MIA and preinvasive lesions.

Methods

Patient selection

We retrospectively reviewed data from patients with SSNs for whom a definitive pathological diagnosis was obtained between October 2010 and December 2015. The inclusion criteria were as follows: (I) at least one SSN with a diameter ≤3 cm detected by HRCT; (II) pGGNs or PSNs with a maximum diameter of the solid component ≤5 mm; (III) surgical resection and HRCT examination within 1 month before the operation; and (IV) complete clinical and pathological data. The exclusion criteria were as follows: (I) benign lesions confirmed by pathological diagnosis, such as fibrosis or chronic inflammation; (II) diffuse GGOs and a suspicion of interstitial lung disease, fibrotic changes, or bronchiolitis; (III) failure to undergo HRCT within 1 month before the operation; and (IV) SSNs that automatic and accurate measurement of the three-dimensional volume could not be performed.

Finally, 316 SSNs from 287 patients, of which 260 were pGGNs, 47 were PSNs with solid components ≤5 mm, and nine were ground-glass nodules (GGNs) with cystic airspaces, were included in this study. The Institutional Review Board approved this study, while the requirement for informed consent was waived, given the retrospective nature of the study.

CT examination

All CT scans were obtained using 64-detector row scanners (LightSpeed VCT, Discovery CT750 HD, or Optima CT660, General Electric Medical Systems, Milwaukee, WI; TOSHIBA Aquilion, TOSHIBA Medical Systems) and an unenhanced or enhanced helical technique at full inspiration. The CT parameters were as follows: tube voltage, 120 kVp; auto mA settings [tube current, approximately 200–350 mA; noise index, 13; pitch, 0.992 or 0.984; rotation time, 0.5 s; thickness, 5 mm; lung window width of 1,600 Hounsfield units (HU) and level of –600 HU; mediastinal window width of 360 HU and

level of 60 HU]. Reconstruction thicknesses were 1.25 or 1.0 mm, and the intervals were 0.8 mm using a standard reconstruction algorithm. For enhanced CT scans, iopromide injection (iodine concentration 300 mg/mL) at a dose of approximately 80–90 mL and a flow rate of 2.5 mL/s was used as the contrast material. Images were obtained 35 s after the intravenous injection. All images were transmitted to the GE Healthcare AW 4.6 workstation for post-processing.

Image acquisition and analysis

Two radiologists (L Qi and W Lu, with two and three years of experience in chest CT, respectively) independently reviewed all enrolled images. Both radiologists were blinded to the patients' detailed clinicopathological information. Disagreements were resolved through consultation with a senior radiologist (J Wang with 22 years of experience in chest CT).

We evaluated imaging data on multi-planar reformation images, including the lesion location, mean diameter, mean and relative CT values, volume, mass, and morphological features (including lobulated, spiculated, and vacuole signs; air bronchogram, pleural tag, or pleural indentation sign).

The mean diameter of each nodule was defined as the average of its maximal length and maximal orthogonal diameter, measured with electronic calipers on transverse CT sections that included the largest cross-sectional area of the nodule at the lung window. The maximum diameter of the solid component of a PSN was measured using the electronic caliper at the lung window. The attenuation of each SSN was measured at the maximum cross-sectional area of the nodule on transverse CT sections at the lung window, excluding portions of apparent vessels; and the mean CT value was calculated as the average of two measurements. The relative CT value was calculated as the ratio of the mean CT value at the maximum level of the lesion to the corresponding value of normal lung tissue at the same level to reduce the influence of the different inspiratory status and contrast medium on CT values.

The SSN volume was calculated at a workstation (Advantage Workstation 4.6, GE) using Lung VCAR software (GE Medical Systems). Segmentation was completed automatically, and the volume was also calculated automatically after the radiologist had placed a marker on the nodule. A three-dimensional template was presented, showing the nodule in an optimal manner. The SSN mass was calculated by the following equation: $M = V \cdot (A + 1{,}000)/1{,}000$, where M is the mass in mg, V is the volume in mm^3, and A is the mean attenuation in HU (30).

Pathological diagnosis

All enrolled pathological specimens were reviewed by a senior pathologist (L Yang, with more than 10 years of experience in diagnosing thoracic tumors). Histological diagnoses followed the 2015 World Health Organization classification of lung adenocarcinomas and classified as atypical adenomatous hyperplasia (AAH), AIS, MIA, and IAC (8). IACs are classified by their predominant pattern after using comprehensive histological subtyping based on lepidic, acinar, papillary, micropapillary, and solid patterns. Variants include invasive mucinous adenocarcinoma, colloid, fetal, and enteric adenocarcinoma (8).

In this study, we classified pre-invasive lesions (including AAH and AIS) and MIAs as group A with similar and better prognosis, and IACs as group B.

Statistical analysis

All statistical tests were performed using SPSS version 19.0 (IBM Corp., Armonk, NY). Tests of normality for continuous data used Kolmogorov-Smirnov test. Normally distributed data are expressed as mean ± standard deviation, while abnormally distributed data are expressed as median (range). The patients' sex, lesion location, and morphological characteristics were analyzed for differences between the two groups or among the three IAC subtypes using Pearson's chi-squared test. Differences in patients' age between the groups were analyzed using independent samples t test, and comparisons of the mean diameter, mean and relative CT values, and SSN volume and mass between the groups were performed using the Mann-Whitney U test. The above measured data were also analyzed for differences among the three IAC subtypes including lepidic, acinar, and papillary predominant adenocarcinomas using one-way analysis of variance or the Kruskal-Wallis test. In addition, binary logistic regression analysis was performed to estimate IAC likelihood. In binary logistic regression analysis, groups A and B were regarded as dependent variables, while statistically significant variables in univariate analyses were regarded as independent variables. Finally, receiver operating characteristic (ROC) analyses were conducted for statistically significant variables in the binary logistic regression to draw ROC curves; the optimal cutoff values were then confirmed. P values <0.05 were considered

Table 1 Clinical and radiological characteristics of the 287 patients and 307 SSNs

Variable	AAH/AIS/MIA	IAC	P value
Number	112	195	N/A
Age	52.8±9.5	56.4±9.5	0.001[a]
Sex			0.078[c]
Male	16	44	
Female	96	151	
Location			0.475[c]
RUL	41	76	
RML	12	17	
RLL	21	26	
LUL	29	50	
LLL	9	26	
Morphologic features			
Lobulated sign	55	161	<0.001[c]
Spiculated sign	6	26	0.028[c]
Vacuole sign/air bronchogram	15	84	<0.001[c]
Pleural tag/pleural indentation sign	35	88	0.017[c]
Mean diameter (mm)	7.75 (3.5–16.0)	11.6 (5.0–25.6)	<0.001[b]
Mean CT value (HU)	–591.5 (–770 to 389)	–538 (–738 to 212)	<0.001[b]
Relative CT value	0.69 (0.46–0.87)	0.63 (0.24–0.84)	<0.001[b]
Volume (mm^3)	250 (28–2,136)	890 (89–7,786)	<0.001[b]
Mass (mg)	98.9 (11.7–803.1)	432.8 (37.5–3,706.1)	<0.001[b]

Sex, location and morphological features are expressed in terms of frequency; age is expressed as mean ± standard deviation; the mean diameter, mean CT value, relative CT value, volume and mass are expressed as median (range). [a], *t*-test; [b], Mann-Whitney *U*-test; [c], Pearson χ^2 test. In the table, SSNs were taken as the study object. Therefore, some patients with multiple resected SSNs were double-counted. AAH, atypical adenomatous hyperplasia; AIS, adenocarcinoma in situ; MIA, minimally invasive adenocarcinoma; IAC, invasive adenocarcinoma; RLL, right lower lobe; RML, right middle lobe; RUL, right upper lobe; LLL, left lower lobe; LUL, left upper lobe; CT, computed tomography; HU, Hounsfield units.

statistically significant.

Results

Clinical and radiological characteristics of the 287 patients and 307 pulmonary SSNs are summarized in *Table 1*. Among the patients, 229 were female and 58 were male (mean age, 55.1±9.5 years; age range, 26 to 77 years); 230 patients underwent asymptomatic screening, 44 patients had physical symptoms such as fever, cough, expectoration, and chest pain; and 13 patients had a history of cancer, including one with submandibular gland carcinoma, one with gastric cancer, one with nasopharyngeal carcinoma, one with gingival cancer, one with rectal cancer, one with lung cancer, three with thyroid carcinomas, and four with breast cancer.

SSNs included 260 pGGNs, 47 PSNs with solid component ≤5 mm, and nine GGNs with cystic airspaces. The latter were not suitable for volume and mass analysis, so we analyzed them individually. The mean diameter was ≤20 mm in 303 SSNs (303/316, 95.9%).

According to the pathological analysis, the nine separately analyzed GGNs with cystic airspaces proved to be IACs. The remaining 307 SSNs were divided into two groups: group A included AAHs (n=15), AISs (n=56), and

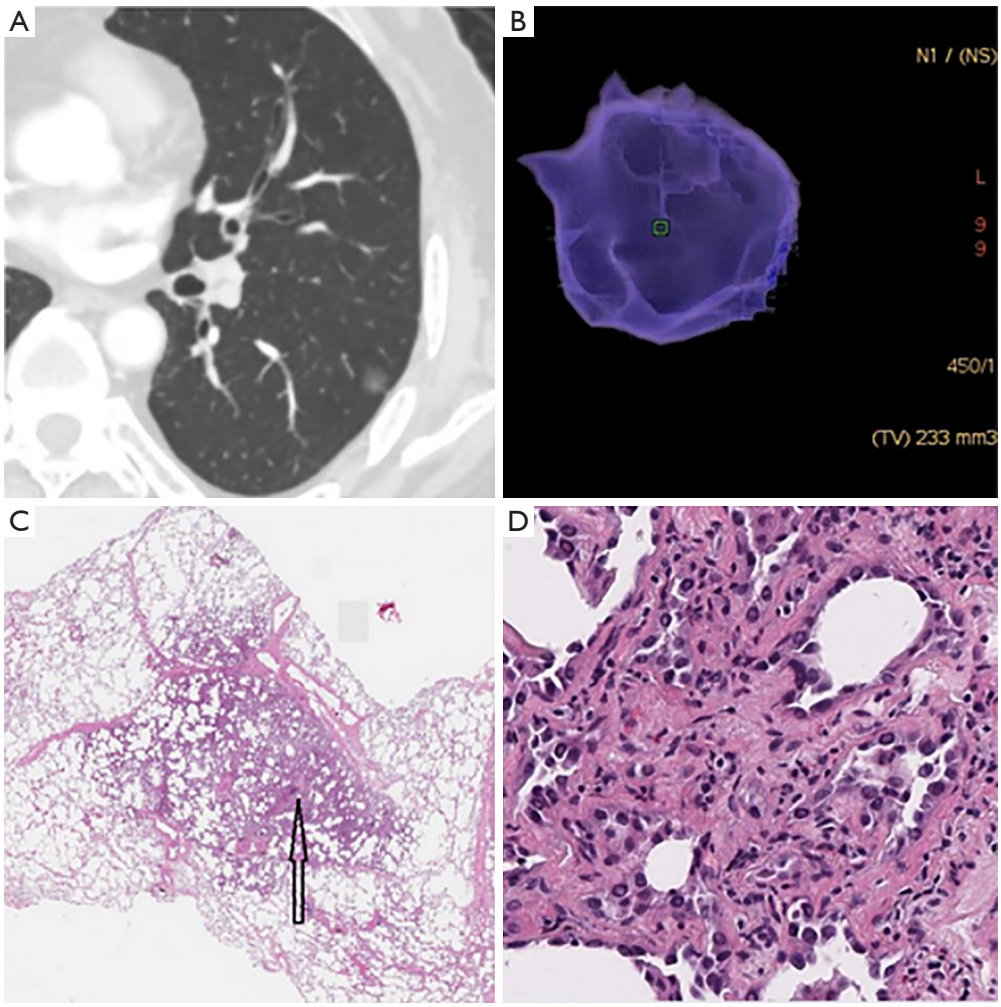

Figure 1 Minimally invasive adenocarcinoma (MIA) in a 62-year-old woman. (A) The axial CT image reveals a pGGN with the diameter of 9.7 mm × 8.9 mm and with slight lobulation and adhesion to the pleura in left lower lobe; (B) the three-dimensional volume of the pGGN was 233 mm^3, then we calculated that its mass was 80 mg; (C) low-magnification of the histologic specimen (Hematoxylin Eosin, 40×) shows darkly stained region (black arrow); (D) high-magnification of the histologic specimen (Hematoxylin Eosin, 200×) shows a small amount of tumor cells infiltrate the lung interstitial tissue with invasion thickness ≤5 mm. CT, computed tomography; pGGN, pure ground-glass nodule.

MIAs (n=41), for a total of 112 SSNs; and group B included 195 IACs (predominant pattern: lepidic, n=100; acinar, n=76; papillary n=19; *Figures 1,2*).

SSN size distribution

Among the 260 pGGNs, 81, 57, 89, and 33 had a mean diameter <8, 8–10, 10–15, and >15 mm, respectively. The pathological types of these pGGNs included 15 AAHs (5.8%), 54 AISs (20.8%), 32 MIAs (12.3%), and 159 IACs (61.1%). The distribution of pathological subtypes of pGGNs with different diameters is summarized in *Figure 3*.

The mean diameter of the 47 PSNs was 11.9±3.8 mm and of the solid component was 3.1±0.9 mm. Among the PSNs with solid component ≤5 mm, two (4.3%) were AISs, nine (19.1%) were MIAs, and 36 (76.6%) were IACs.

Demographic data and SSN location and morphological features

There was no significant difference in either patient sex (P=0.078) or lesion location (P=0.475) between group A and

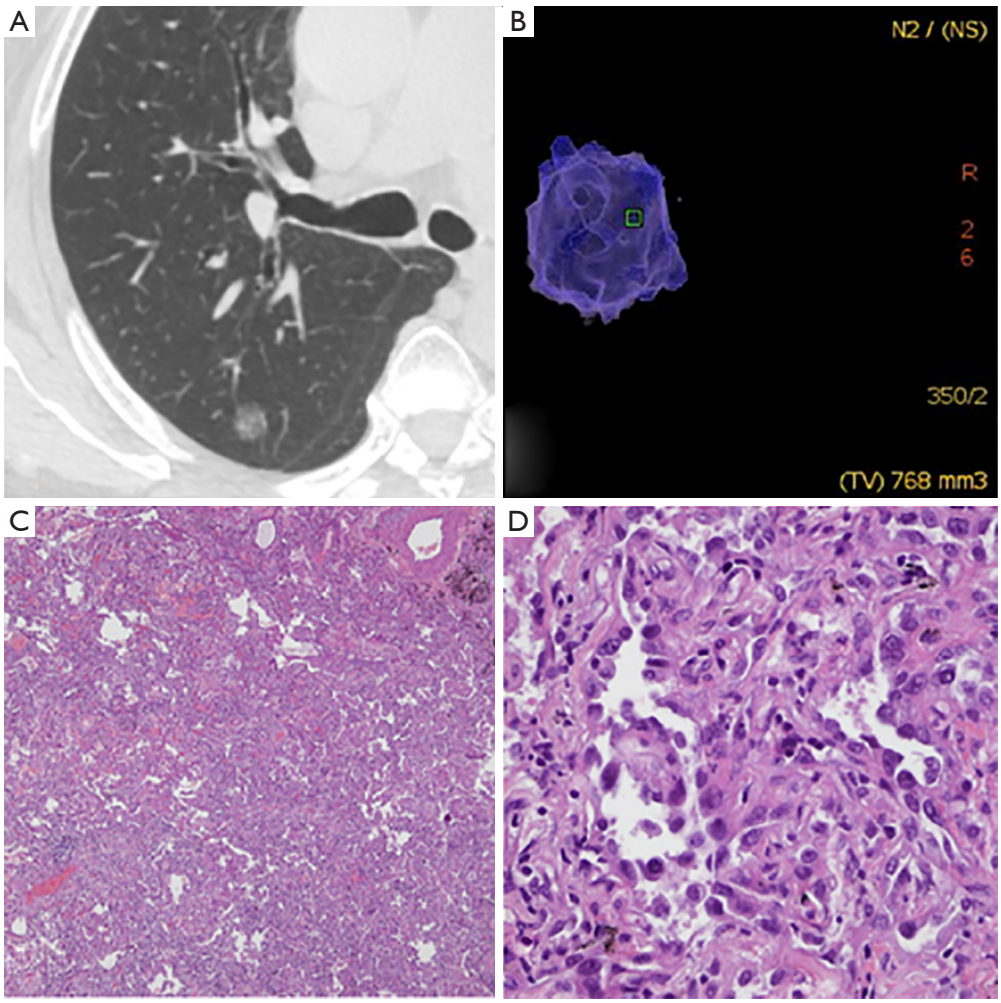

Figure 2 Invasive adenocarcinoma (IAC) with lepidic predominant pattern in a 70-year-old woman. (A) The axial CT image reveals a pGGN in the right upper lobe. The pGGN was relatively larger diameter in 12.3 mm × 9.6 mm; (B) the three-dimensional volume of the pGGN was 768 mm^3, then we calculated that its mass was 362 mg; (C) low-magnification of the histologic specimen (Hematoxylin Eosin, 40×) shows darkly stained region; (D) high-magnification of the histologic specimen (Hematoxylin Eosin, 400×) shows tumor cells grow along the alveolar wall and infiltrate the lung interstitial tissue with invasion thickness >5 mm. CT, computed tomography; pGGN, pure ground-glass nodule.

B, while patient age in group B was older than that in group A (56.4±9.5 *vs.* 52.8±9.5 years, P=0.001).

Regarding the morphological features, statistically significant differences between the groups were found in lobulated (P<0.001), spiculated (P=0.028), and vacuole or air bronchogram signs (P<0.001), and in pleural tag or pleural indentation sign (P=0.017); and IAC was more likely to present these signs.

Regarding SSN data, we found significant differences between the groups in the mean diameter, mean and relative CT value, volume, and mass (P<0.001 for all; *Table 1*).

Binary logistic regression and ROC curve analyses

By binary logistic regression analysis, we found that SSN mass (odds ratio, 1.007; P<0.001) was the only important indicator for IAC diagnosis. As the SSN mass increased by 1 mg, the risk of IAC increased by 1.007-fold (*Table 2*). According to ROC curve analysis, the optimal cutoff value of the SSN mass was 283.2 mg [area under curve (AUC): 0.859; sensitivity: 68.7%; specificity: 92.9%] for differentiating IACs from MIAs, AISs, and AAHs (*Figure 4*).

Analysis of clinical data and HRCT features of IAC subtypes

In this study, IAC subtypes included lepidic, acinar, and papillary adenocarcinomas. There were no significant differences among the three subtypes regarding the patients' age and sex; lesion location, mean diameter, volume, and mass; and the HRCT features of lobulated, spiculated, and of pleural tag/indentation. In contrast, significant differences among subtypes were found for vacuole sign/air bronchogram (P=0.032) and both mean (P<0.001) and relative (P<0.001) CT values (*Table 3*).

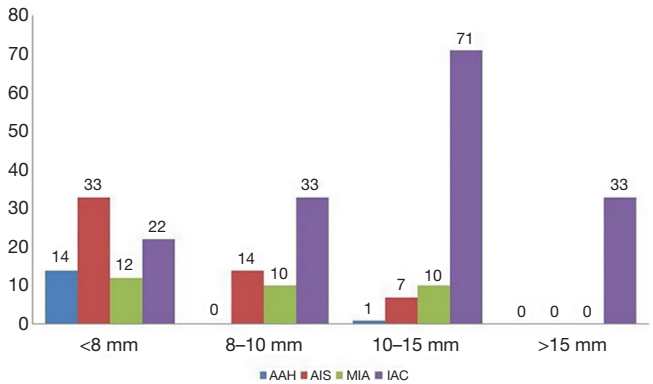

Figure 3 The distribution of pathological subtypes of pGGNs with different diameters. The pathological types of 260 pGGNs included 15 AAHs (5.8%), 54 AISs (20.8%), 32 MIAs (12.3%), and 159 IACs (61.1%). Among the 15 AAHs, 93.3%, 0%, 6.7%, and 0% had a mean diameter <8, 8–10, 10–15, and >15 mm, respectively. Among the 54 AISs, the respective percentages were 61.1%, 25.9%, 13.0%, and 0%; among the 32 MIAs, they were 37.5%, 31.25%, 31.25%, and 0%; and among the 159 IACs, they were 13.8%, 20.7%, 44.7%, and 20.8%. pGGN, pure ground-glass nodule; IAC, invasive adenocarcinoma; MIA, minimally invasive adenocarcinoma; AIS, adenocarcinoma in situ; AAH, atypical adenomatous hyperplasia.

Morphological and pathological features of GGNs with cystic airspaces

We defined GGNs with cystic airspaces as cavitary lesions in which ground glass components appeared abutting or in the wall of the cystic airspace. Cyst diameter (>5 mm)

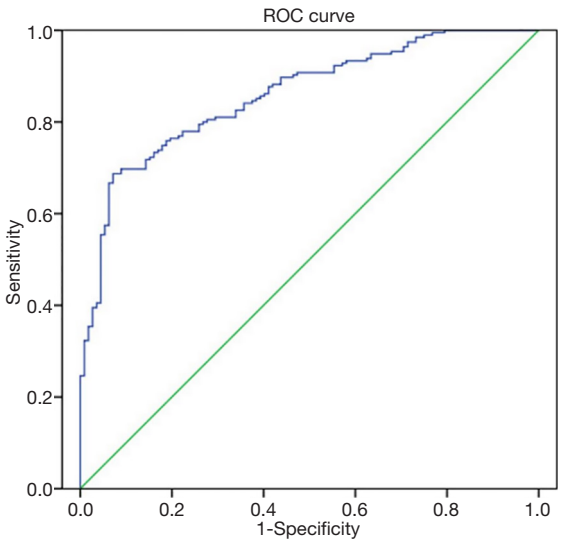

Area under the curve

Test result variable(s): mass

Area	Std. error[a]	Asymptotic Sig.[b]	Asymptotic 95% Confidence interval	
			Lower bound	Upper bound
0.859	0.021	0.000	0.818	0.900

Figure 4 ROC curve for SSN mass: IAC demonstrate a significantly greater mass than that of MIA/AIS/AAH, with an optimal cutoff value of 283.2 mg [area under curve (AUC): 0.859; sensitivity: 68.7%; specificity: 92.9%; 95% confidence interval: 0.818, 0.900]. [a], under the nonparametric assumption; [b], null hypothesis: true area =0.5. SSN, subsolid nodule; IAC, invasive adenocarcinoma; MIA, minimally invasive adenocarcinoma; AIS, adenocarcinoma in situ; AAH, atypical adenomatous hyperplasia.

Table 2 Independent predictor of IAC in the binary logistic regression analysis

Independent variables and constant	Variables in the equation							
	B	S.E	Wals	df	Sig.	Exp (B)	Exp (B) 95% CI	
							Lower	Upper
Mass (mg)	0.007	0.001	50.684	1	0.000	1.007	1.005	1.009
Constant	–1.319	0.240	30.301	1	0.000	0.267	–	–

B, regression coefficient; SE, standard error; Wals, chi-square value; df, degrees of freedom; Sig, significance; Exp(B), odds ratio. CI, confidence interval; CT, computed tomography; HU, Hounsfield units.

Table 3 Clinical data and HRCT features of IAC subtypes

Variable	Lepidic adenocarcinoma	Acinar adenocarcinoma	Papillary adenocarcinoma	P value
Number	100	76	19	N/A
Age	57.3±10.3	55.5±9.0	54.7±6.4	0.334[d]
Sex				0.700[c]
Male	25	15	4	
Female	75	61	15	
Location				0.112[c]
RUL	44	27	5	
RML	9	3	5	
RLL	11	12	3	
LUL	24	23	3	
LLL	12	11	3	
Morphologic features				
Lobulated sign	83	63	15	0.909[c]
Spiculated sign	9	15	2	0.108[c]
Vacuole sign/air bronchogram	34	40	10	0.032[c]
Pleural tag/pleural indentation sign	47	30	11	0.305[c]
Mean diameter (mm)	11.6 (5.0–25.6)	11.6 (5.8–24.3)	12.1 (7.7–17.0)	0.887[e]
Mean CT value (HU)	–570 (–738 to 263)	–512 (–720 to 212)	–457 (–656 to 255)	<0.001[e]
Relative CT value	0.65±0.11	0.59±0.12	0.54±0.13	<0.001[d]
Volume (mm^3)	867.5 (89–7,430)	981.5 (101–7,786)	908 (234–3,801)	0.866[e]
Mass (mg)	373.8 (37.5–3,141.3)	489.3 (50.1–3,706.1)	559.8 (90.6–2,360.4)	0.306[e]

Sex, location and morphological features are expressed in terms of frequency; age and relative CT value are expressed as mean ± standard deviation; the mean diameter, mean CT value, volume and mass are expressed as median (range). [c], Pearson χ^2 test; [d], one-way analysis of variance (ANOVA); [e], Kruskal-Wallis test. RLL, right lower lobe; RML, right middle lobe; RUL, right upper lobe; LLL, left lower lobe; LUL, left upper lobe; CT, computed tomography; HU, Hounsfield units.

differed from vacuole diameter (1–3 mm) (*Figure 5*). Most cavities were irregular, round, or round-like, with large tension, and an irregular wall. All nine GGNs with cystic airspaces were identified to be IACs.

Discussion

We examined whether the qualitative and quantitative imaging features of SSNs can differentiate IAC from MIA and preinvasive lesions. We found that SSN mass was the only independent risk factor for IAC, with an optimal cutoff value of 283.2 mg (sensitivity, 68.7%; specificity, 92.9%).

Notably, we only enrolled resected pGGNs with diameters ≤3 cm, and resected PSNs with overall diameters ≤3 cm and solid components ≤5 mm. There are three main reasons for the inclusion criteria: Firstly, the cut-off diameter value for distinguishing pulmonary nodule from mass was 3 cm. Compared to recommendations for SSNs with diameters >3 cm, there is much controversy for managing that with diameters ≤3 cm. Secondly, pGGNs from 0.6–3 cm can be radiologically staged as clinical AIS; a pGGN >3 cm is considered lepidic predominant adenocarcinoma. PSNs with overall diameters ≤3 cm and solid components ≤5 mm are considered cT1mi (MIA); and if the solid components of PSNs are >5 mm, the T staging is determined by the diameter of the solid component (32). Thirdly, in clinical practice, we found pGGNs and PSNs with solid components ≤5 mm have similar biological

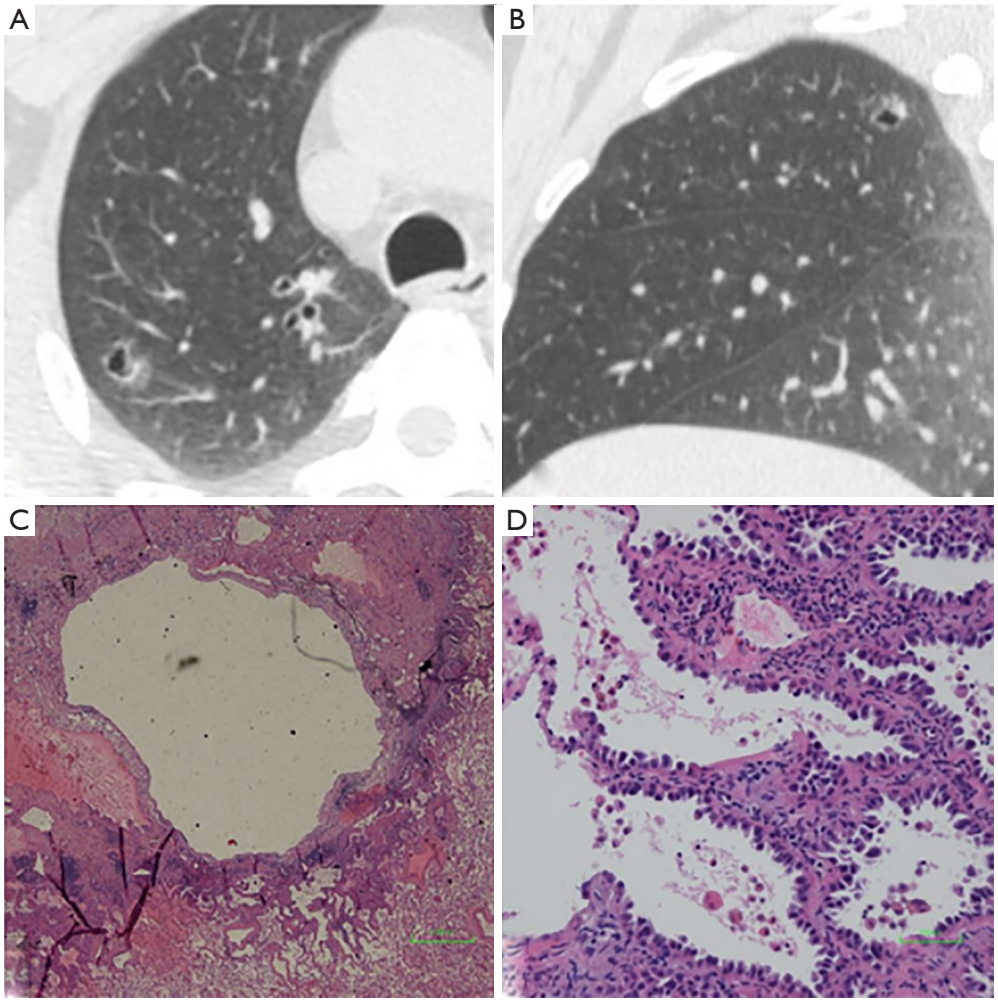

Figure 5 GGN with cystic airspace in a 53-year-old woman. (A) Axial and (B) sagittal CT image show a thin-walled cavitary GGN with the diameter of 13.7 mm × 11.3 mm in right upper lob. (C) Low-magnification (Hematoxylin Eosin, 40×) and (D) high-magnification (Hematoxylin Eosin, 200×) of the histologic specimen show an irregular cystic cavity and tumor cells grow along the pre-existing alveolar wall. GGN, ground-glass nodule; CT, computed tomography.

behavior, therefore, we put them together.

Mass can simultaneously reflect the volume and density of pulmonary nodules, thus reflecting nodule characteristics more accurately (31). Therefore, mass can help distinguish IACs among SSNs with potentially superior accuracy to diameter, density, or volume. In this study, we found that the cutoff mass of 283.2 mg was optimal for differentiating IACs from AAHs/AISs/MIAs. However, Lim *et al.* (17) reported that the most significant cutoff mass for differentiating IACs from AISs/MIAs was 0.472 g, and Liu *et al.* (22) reported that the most significant cutoff mass for differentiating IACs from AAHs/AISs/MIAs was 386 mg. This discrepancy may be due to differences in the type and size of the enrolled SSNs. In our study, we enrolled pGGNs with diameters ≤3 cm and PSNs with overall diameters ≤3 cm and solid components ≤5 mm, whereas Lim *et al.* (17) only enrolled pGGNs with diameters ≥1 cm and did not enroll AAHs; Liu *et al.* (22) reported a cutoff mass of 386 mg to differentiate IACs from AAHs/AISs/MIAs only for pGGNs. Moreover, Son *et al.* (24) reported that the mass significantly differed between IACs and MIAs or AISs on univariate analysis; however, it did not significantly differ on multivariate analysis.

Regarding the morphological features, our univariate analysis showed that lobulated, spiculated, and vacuole/air bronchogram signs, as well as pleural retraction significantly

differed between the IAC and AAH/AIS/MIA groups. However, on binary logistic regression analysis, these morphological features did not significantly differ between the two groups, in line with the results of two previous studies (15,17). However, other studies showed different results. For example, Hu *et al.* (18) and Fan *et al.* (19) showed that lobulation and pleural indentation were important predictors for malignant diagnosis of SSNs. Moon *et al.* (13), Si *et al.* (16), and Zhao *et al.* (21) showed that pleural indentation was a risk factor of IAC, while Zhao *et al.* (21) also showed that lobulation was a risk factor of IAC.

In this study, we found that the most common pathological type among the pGGNs and PSNs with solid components ≤5 mm was the IAC (61.1% and 76.6%, respectively), which differed from the findings of previous studies (12-17,19,20), but was consistent with the findings of the several previous studies (18,21,22,24-26). These differences might be explained by three reasons. First, the type and size of enrolled SSNs were different among studies; second, the surgical indication of SSNs in our hospital was more stringent, and many resected SSNs had lobulated, spiculated, or vacuole sign, bronchogram, or pleural retraction, and therefore the proportion of IACs was higher; finally, SSNs may be associated with a higher degree of malignancy in Asia, which requires further study. In addition, we found that all AAHs and most AISs appeared as pGGNs on HRCT. AISs also appeared as PSNs on HRCT (3.6%), possibly due to the collapse of alveolar walls and elastosis or benign scarring (33,34). Similarly, the pathological types of pGGNs included MIAs and IACs, in agreement with the findings of previous studies (12-21,33).

In pGGNs, we found that the mean diameter of most AAHs were <8 mm, and only one AAH had a diameter >10 mm. The mean diameters of all AISs and MIAs were <15 mm, whereas MIAs were evenly distributed among the <8-mm (n=12), 8–10-mm (n=10), and 10–15-mm (n=10) diameter groups. However, a previous study reported that MIAs usually appear as pGGNs of ≥10 mm in diameter on HRCT (20). This discrepancy may be due to the different study population and inter-observer variability among different pathologists (9).

We also explored HRCT features of IAC subtypes including lepidic, acinar, and papillary adenocarcinomas and found that vacuole sign/air bronchogram, as well as the mean and relative CT values significantly differed among subtypes. However, there were no significant differences among the three IAC subtypes in mean diameter, volume, and mass. In our sample, vacuole sign/air bronchogram was the most common feature in patients with papillary adenocarcinoma, and the mean CT value for this type was the highest. Although SSN mass did not significantly differ among the three subtypes, it was highest in papillary adenocarcinoma.

Moreover, deep learning technology in the field of artificial intelligence has made rapid progress. Wang *et al.* (35) explored the performance of an automatic classification framework based on a 3D convolutional neural network (CNN) in distinguishing IAC from AAH/AIS/MIA, and they found the performance of the deep CNN was superior to that of experienced radiologists. We will explore it further in our next study.

Several limitations in our study should be mentioned. First, it included a retrospective design, so there was a certain bias in the selection of cases. We only enrolled surgical SSNs and excluded SSNs with a long-term follow-up period but no surgical intervention. Moreover, we excluded SSNs with diameters >3 cm and PSNs with solid components >5 mm. However, our study could help radiologists and surgeons distinguish IACs in SSNs and develop an appropriate management strategy in clinical practice. Second, despite our relatively large study population, the number of PSNs was relatively small; thus, further investigations are warranted. Third, we mainly focused on the resected SSNs rather than that with long-term follow-up. Watchful waiting with annual or biannually follow up until 5 years policy is appropriate for pGGNs (4). However, we included these SSNs resected before December 2015, and retrospectively reviewed these data to explore the role of qualitative and quantitative imaging features of SSNs in differentiating IAC, which would be helpful in deciding the optimal management and evaluating prognosis, especially for anxious patients. Finally, 85 SSNs (85/392, 21.7%) failed to be accurately segmented by the Lung VCAR software, possibly because of the lower density, adjacent structures, including vascular and pleura, and the software itself. However, the 85 SSNs were excluded from our study.

In summary, we propose that the SSN mass is a reliable predictor for differentiating IAC from AAH/AIS/MIA, and its optimal cutoff value is 283.2 mg (AUC: 0.859; sensitivity: 68.7%; specificity: 92.9%).

Acknowledgments

We would like to thank Mr. Chang-Fa Xia (National Office for Cancer Prevention and Control, National Cancer

Center/National Clinical Research Center for Cancer/Cancer Hospital, Chinese Academy of Medical Sciences and Peking Union Medical College, Beijing, China) for his statistical assistance. We would like to thank Editage (www.editage.cn) for English language editing.
Funding: This work supported by the National Key R&D Program of China (grant number 2017YFC1308700); the National Natural Science Foundation of China (grant number 81171344); and Chinese Academy of Medical Sciences Initiative for Innovative Medicine (grant number 2017-I2M-1-005).

Footnote

Conflicts of Interest: The authors have no conflicts of interest to declare.

Ethical Statement: The authors are accountable for all aspects of the work in ensuring that questions related to the accuracy or integrity of any part of the work are appropriately investigated and resolved. The institutional review boards of our hospitals approved this retrospective study and informed consent was waived.

References

1. Siegel RL, Miller KD, Jemal A. Cancer statistics, 2016. CA Cancer J Clin 2016;66:7-30.
2. Lin KF, Wu HF, Huang WC, et al. Propensity score analysis of lung cancer risk in a population with high prevalence of non-smoking related lung cancer. BMC Pulm Med 2017;17:120.
3. Wu FZ, Huang YL, Wu CC, et al. Assessment of Selection Criteria for Low-Dose Lung Screening CT Among Asian Ethnic Groups in Taiwan: From Mass Screening to Specific Risk-Based Screening for Non-Smoker Lung Cancer. Clin Lung Cancer 2016;17:e45-e56.
4. MacMahon H, Naidich DP, Goo JM, et al. Guidelines for management of incidental pulmonary nodules detected on CT images: from the Fleischner society. Radiology 2017;284:228-243.
5. Hansell DM, Bankier AA, MacMahon H, et al. Fleischner Society: glossary of terms for thoracic imaging. Radiology 2008;246:697-722.
6. Kobayashi Y, Sakao Y, Deshpande GA, et al. The association between baseline clinical-radiological characteristics and growth of pulmonary nodules with ground-glass opacity. Lung Cancer 2014;83:61-6.
7. Kim H, Park CM, Koh JM, et al. Pulmonary subsolid nodules: what radiologists need to know about the imaging features and management strategy. Diagn Interv Radiol 2014;20:47-57.
8. Travis WD, Brambilla E, Nicholson AG, et al. The 2015 World Health Organization Classification of Lung Tumors: Impact of Genetic, Clinical and Radiologic Advances Since the 2004 Classification. J Thorac Oncol 2015;10:1243-60.
9. Boland JM, Froemming AT, Wampfler JA, et al. Adenocarcinoma in situ, minimally invasive adenocarcinoma, and invasive pulmonary adenocarcinoma—analysis of interobserver agreement, survival, radiographic characteristics, and gross pathology in 296 nodules. Hum Pathol 2016; 51:41-50.
10. Van Schil PE, Asamura H, Rusch VW, et al. Surgical implications of the new IASLC/ATS/ERS adenocarcinoma classification. Eur Respir J 2012;39:478-86.
11. Tsutani Y, Miyata Y, Nakayama H, et al. Appropriate sublobar resection choice for ground glass opacity-dominant clinical stage IA lung adenocarcinoma: wedge resection or segmentectomy. Chest 2014;145:66-71.
12. Eguchi T, Yoshizawa A, Kawakami S, et al. Tumor size and computed tomography attenuation of pulmonary pure ground-glass nodules are useful for predicting pathological invasiveness. PLoS One 2014;9:e97867.
13. Moon Y, Sung SW, Lee KY, et al. Pure ground-glass opacity on chest computed tomography: predictive factors for invasive adenocarcinoma. J Thorac Dis 2016;8:1561-70.
14. Kitami A, Sano F, Hayashi S, et al. Correlation between histological invasiveness and the computed tomography value in pure ground-glass nodules. Surg Today 2016;46:593-8.
15. Kim HY, Shim YM, Lee KS, et al. Persistent pulmonary nodular ground-glass opacity at thin-section CT: histopathologic comparisons. Radiology 2007;245:267-75.
16. Si MJ, Tao XF, Du GY, et al. Thin-section computed tomography-histopathologic comparisons of pulmonary focal interstitial fibrosis, atypical adenomatous hyperplasia, adenocarcinoma in situ, and minimally invasive adenocarcinoma with pure ground-glass opacity. Eur J Radiol 2016;85:1708-15.
17. Lim HJ, Ahn S, Lee KS, et al. Persistent pure ground-glass opacity lung nodules ≥ 10 mm in diameter at CT scan: histopathologic comparisons and prognostic implications. Chest 2013;144:1291-9.
18. Hu H, Wang Q, Tang H, et al. Multi-slice computed

tomography characteristics of solitary pulmonary ground-glass nodules: Differences between malignant and benign. Thorac Cancer 2016;7:80-7.
19. Fan L, Liu SY, Li QC, et al. Multidetector CT features of pulmonary focal ground-glass opacity: differences between benign and malignant. Br J Radiol 2012;85:897-904.
20. Lee SM, Park CM, Goo JM, et al. Invasive pulmonary adenocarcinomas versus preinvasive lesions appearing as ground-glass nodules: differentiation by using CT features. Radiology 2013;268:265-73.
21. Zhao Q, Wang JW, Yang L, et al. CT diagnosis of pleural and stromal invasion in malignant subpleural pure ground-glass nodules: an exploratory study. Eur Radiol 2019;29:279-86.
22. Liu Y, Sun H, Zhou F, et al. Imaging features of TSCT predict the classification of pulmonary preinvasive lesion, minimally and invasive adenocarcinoma presented as ground glass nodules. Lung Cancer 2017;108:192-7.
23. Yu J, Zhu S, Ge Z, et al. Multislice spiral computed tomography in the differential diagnosis of ground-glass opacity. J Cancer Res Ther 2018;14:128-32.
24. Son JY, Lee HY, Lee KS, et al. Quantitative CT analysis of pulmonary ground-glass opacity nodules for the distinction of invasive adenocarcinoma from pre-invasive or minimally invasive adenocarcinoma. PLoS One 2014;9:e104066.
25. Wu FZ, Chen PA, Wu CC, et al. Semiquantitative Visual Assessment of Sub-solid Pulmonary Nodules 3 cm in Differentiation of Lung Adenocarcinoma Spectrum. Sci Rep 2017;7:15790.
26. Revel MP, Mannes I, Benzakoun J, et al. Subsolid Lung Nodule Classification: A CT Criterion for Improving Interobserver Agreement. Radiology 2018;286:316-25.
27. Chen PA, Huang EP, Shih LY, et al. Qualitative CT Criterion for Subsolid Nodule Subclassification: Improving Interobserver Agreement and Pathologic Correlation in the Adenocarcinoma Spectrum. Acad Radiol 2018;25:1439-45.
28. Hsu HT, Tang EK, Wu MT, et al. Modified Lung-RADS Improves Performance of Screening LDCT in a Population with High Prevalence of Non-smoking-related Lung Cancer. Acad Radiol 2018;25:1240-51.
29. Oda S, Awai K, Murao K, et al. Computer-aided volumetry of pulmonary nodules exhibiting ground-glass opacity at MDCT. AJR Am J Roentgenol 2010;194:398-406.
30. Oda S, Awai K, Murao K et al. Volume-doubling time of pulmonary nodules with ground glass opacity at multidetector CT: Assessment with computer-aided three-dimensional volumetry. Acad Radiol 2011;18:63-9.
31. de Hoop B, Gietema H, van de Vorst S, et al. Pulmonary ground-glass nodules: increase in mass as an early indicator of growth. Radiology 2010; 255:199-206.
32. Lim W, Ridge CA, Nicholson AG, et al. The 8th lung cancer TNM classification and clinical staging system: review of the changes and clinical implications. Quant Imaging Med Surg 2018;8:709-18.
33. Travis WD, Asamura H, Bankier AA, et al. The IASLC Lung Cancer Staging Project: Proposals for Coding T Categories for Subsolid Nodules and Assessment of Tumor Size in Part-Solid Tumors in the Forthcoming Eighth Edition of the TNM Classification of Lung Cancer. J Thorac Oncol 2016;11:1204-23.
34. Yamada N, Kusumoto M, Maeshima A, et al. Correlation of the solid part on high-resolution computed tomography with pathological scar in small lung adenocarcinomas. Jpn J Clin Oncol 2007;37:913-7.
35. Wang S, Wang R, Zhang S, et al. 3D convolutional neural network for differentiating pre-invasive lesions from invasive adenocarcinomas appearing as ground-glass nodules with diameters ≤3 cm using HRCT. Quant Imaging Med Surg 2018;8:491-9.

Cite this article as: Qi L, Lu W, Yang L, Tang W, Zhao S, Huang Y, Wu N, Wang J. Qualitative and quantitative imaging features of pulmonary subsolid nodules: differentiating invasive adenocarcinoma from minimally invasive adenocarcinoma and preinvasive lesions. J Thorac Dis 2019;11(11):4835-4846. doi: 10.21037/jtd.2019.11.35

